

Polyimide-based aerogel foams, via emulsion-templating

Nicholas Teo, Zipeng Gu, Sadhan C. Jana*

Department of Polymer Engineering, The University of Akron, 250 South Forge Street, Akron, OH, 44325-0301, USA



HIGHLIGHTS

- Oil-in-oil emulsion templating produces aerogel foams from polyimides.
- PEO-PPO-PEO block copolymer surfactant stabilizes oil-in-oil emulsions.
- Surfactant reduces macrovoid size but increases polyimide strand size.
- Surfactant organizes to produce higher contact angle and promotes oil absorption.

ARTICLE INFO

Keywords:
Aerogels
Aerogel foams
Polyimide
Oil-in-oil emulsions
Emulsion-templating

ABSTRACT

An oil-in-oil emulsion-templating method is used to fabricate polyimide aerogel foam materials. These materials contain micrometer size voids (macrovoids) in conjunction with inherently produced meso- and macropores in polyimide gels. Polyamic acid is first synthesized from diamines and dianhydrides and then chemically imidized to obtain a sol. An immiscible oil-type dispersed phase is introduced in the sol via emulsification and the sol is subsequently allowed to transition into a gel, thereby locking the dispersed phase droplets within the structure. The gel is subsequently dried under supercritical conditions to obtain aerogel foams. This paper evaluates the stability of the oil-in-oil emulsion used for templating with reference to the gel times of the continuous phase. Specifically, the effects of surfactant concentration on macrovoid size, mesopore size, and mechanical properties of the aerogel foams are investigated. In addition, water and oil absorption behavior of the aerogel foams are studied.

1. Introduction

Polyimides were first reported in 1908, although its usage increased after the late 1950s once high molecular weight polyimides were successfully prepared [1]. These materials possess excellent properties such as high thermal, hydrolytic, and radiation stability, as well as good mechanical strength and electrical properties at elevated temperatures [2,3]. These properties, in conjunction with its gel forming capability, have qualified polyimides as an appropriate candidate for aerogel fabrication. Polyimide aerogels and their hybrids have been reported in literature [4]. For example, the network structure of silica aerogels were coated with a layer of polyimide to impart structural integrity and improve load bearing capabilities [5]. The step-growth nature of polyimide synthesis also accommodates a variety of monomers for tailoring the mechanical properties, shrinkage, and surface energy of polyimide aerogels [6,7]. Traditionally, polyimides are fabricated using the Dupont two-step process. First, polyamic acids are obtained by reacting dianhydrides and diamines. The second step involves chemical

imidization using acetic anhydride as a dehydrating agent and pyridine as a catalyst, whereby the amic acid functional group is converted to the imide functional group [8]. Other synthesis routes for polyimide aerogels have also been reported, such as ring opening polymerization [9] and substituting isocyanates for amines [10].

Aerogels are frequently fabricated in a cylindrical monolith shape, although recent studies have reported both flexible films and micro-particle forms [11,12]. The high thermal stability and the close proximity of aerogel pore sizes to the mean free path of air molecules impart excellent thermal insulation properties in polyimide aerogels. This has seen polyimide aerogels deployed as insulation for entry/re-entry vehicles and extravehicular activity suits [13]. The inherent low dielectric properties of polyimide aerogels also make them suitable for fabrication of antenna [14,15] and membrane separators for batteries [16]. In addition, the open pore structures of polyimide aerogels, with both meso- (dia 2–50 nm) and macropores (dia > 50 nm), have shown to be useful in filtering airborne nanoparticles. These aerogels have been shown to achieve a high separation efficiency of 99.99%, while

* Corresponding author.

E-mail address: janas@uakron.edu (S.C. Jana).

maintaining high air permeability values $\sim 1 \times 10^{-10} \text{ m}^2$ [17].

The work of Zhai and Jana [17] established strong mesopore fraction vs. filtration efficiency and macropore fraction vs. air permeability relationships. This study's takeaway was that high air permeability and high filtration efficiency require high fractions of macropores and mesopores respectively. However, aerogel monoliths prepared by the methods reported in literature do not allow independent control of both meso- and macropore fractions. This necessitated another method of incorporating macropore fractions in aerogel materials without altering the mesopore content, bearing in mind that the final structures should be one-component, free-standing, and hierarchical. This served as the motivation for the development of aerogel foams, fabricated via inclusion of micrometer sized voids, defined as macrovoids, into inherently porous aerogel structures. The macrovoids allow quick transfer of fluids through the aerogel structures, thus allowing higher fluid permeability.

Aerogel foams have previously been fabricated using a number of methods. Gu and Jana [18] had used a solid template of co-continuous polymer systems to synthesize polyurea aerogel foams. Wang and Jana [19] used a solution of polyethylene oxide to obtain micrometer size voids in syndiotactic polystyrene (sPS) aerogels. Recently, Teo and Jana [20] successfully used a water-in-oil emulsion-templating method to introduce spherical, $\sim 20 \mu\text{m}$ sized macrovoids in macroporous sPS aerogel structures. In this work [20], sPS and a nonionic surfactant were first dissolved in toluene at high temperature and the solution was emulsified using deionized water. The sPS solution turned into a gel when cooled to room temperature, thus locking in the emulsified water droplets within the vitrified structure. The gel was supercritically dried to yield sPS aerogel foam materials. However, this water-in-oil emulsion templating method cannot be extended to water-sensitive monomers such as those encountered in polyimide systems. On the other hand, aerogel foams produced from high temperature polyimides have the potential for expanded applications such as in hot air filtration. In view of this, the present work details an oil-in-oil (O/O) emulsion templating method for incorporation of significant fractions of macrovoids in polyimide aerogel structures. This yields polyimide aerogel foams with macrovoids ($\sim 30 \mu\text{m}$) seen in foams, as well as mesopores found inherently in polyimide aerogels.

2. Experimental section

2.1. Materials

Pyromellitic dianhydride (PMDA) was purchased from Alfa-Aesar (Haverhill, MA) and 2,2'-dimethylbenzidine (DMBZ) was purchased from Shanghai Worldyang Chemical Co. Ltd (Shanghai, China). Tris(2-aminoethyl)amine (TREN) and surfactant F127[®] (trademark of BASF) were purchased from Sigma Aldrich (Milwaukee, WI). Pyridine, acetic anhydride, cyclohexane, and acetone were purchased from Fisher Scientific (Ontario, NY). N,N-dimethylformamide (DMF) was purchased from VWR International (Radnor, PA) and n-heptane was purchased from EMD Millipore (Billerica, MA).

2.2. Fabrication of aerogel foams

An O/O emulsion-templating method was used in this work to obtain micrometer size oil droplets dispersed in the sol. The sol transitioned into a gel, thus locking the emulsified oil droplets within the gel structures. This process resembles the fabrication of polyHIPES [21–23], with the exception that the continuous oil-phase in this study was initially an organic sol, which later turned into a gel with its inherent pores filled by the organic solvent.

All materials were stored in desiccators and used as purchased, with the exception of F127[®] surfactant, which was dried in a vacuum oven for at least 30 min at a temperature of 35 °C prior to dissolution to mitigate the effect of absorbed moisture. The continuous oil phase was

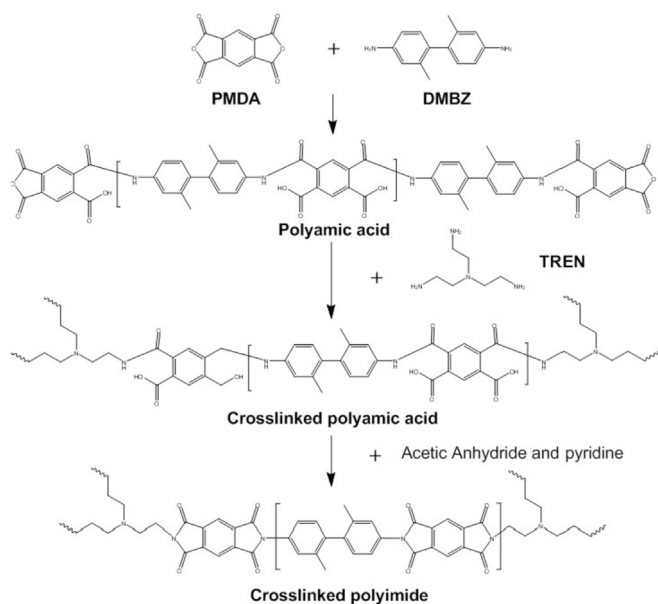


Fig. 1. Reaction scheme for synthesis of polyimide.

first prepared by dissolving PMDA and F127[®] surfactant in DMF over a period of at least 30 min, to ensure full dissolution of the surfactant. DMBZ was dissolved in DMF, added to the PMDA and surfactant solution, and magnetically stirred for 2 min at 1600 rpm to form the polyamic acid solution. TREN, acetic anhydride, and pyridine were added at the same time together to the polyamic acid solution to serve respectively as the crosslinker, dehydrating agent, and catalyst. These three reagents had to be added all at once as the fast reaction kinetics of the crosslinker (TREN) would lead to immediate precipitation of the crosslinked materials if added separately. The reaction was conducted at room temperature of 19 °C in a sealed glass vial under air, with the reaction scheme shown in Fig. 1. The final reaction mixture was stirred magnetically for 3 min followed by addition of the dispersed phase (cyclohexane or n-heptane) and stirred for an additional 5 min. This allowed for the viscosity of the solution to increase with conversion, imparting increased stability to the O/O emulsion. For neat polyimide samples without any surfactant or dispersed phase, this step involved further stirring of only 1.5 min, to allow transfer to the molds before gelation. A typical sample with 30 vol% dispersed phase and 0.5 vol% surfactant based on the continuous phase was prepared from 0.114 g PMDA, 0.017 g F127[®], 0.106 g DMBZ, 0.015 g TREN, 0.360 g acetic anhydride, 0.307 g pyridine, 2.5 mL DMF, and 1.67 mL dispersed phase (cyclohexane or n-heptane). The above recipe produced a polymer concentration of 7.4 wt% in the solution.

The final mixture was poured into cylindrical molds and allowed to gel. The selection of monomers, crosslinker content, and overall polymer concentration in the sol allowed fast gelation and vitrification of the emulsion while facilitating pouring of the sol in the mold. The gels were aged in the molds for 48 h before demolding. The presence of surfactant delayed gelation of the system. Accordingly, the gels were left in the molds for 48 h to ensure completion of crosslinking and imidization reactions. The demolded gels were solvent exchanged sequentially with 25 vol% acetone/75 vol% DMF, 50 vol% acetone/50 vol % DMF, 25 vol% acetone/75 vol% DMF, and finally with 100 vol% acetone at 12-h intervals. In addition, the gels were further washed with 100 vol% acetone for an additional 5 times at 12-h intervals to remove as much of the DMF as possible. The gels were subsequently solvent exchanged with liquid carbon dioxide in an autoclave by washing with 100 vol% liquid carbon dioxide for 6 times at 1.5 h intervals. The liquid carbon dioxide infused gels were subsequently dried under supercritical condition of carbon dioxide at 50 °C and 11 MPa. The surfactant

concentration was varied between 0.5 vol% and 5 vol% to impart stability of the O/O emulsion against creaming and coalescence before gelation of the continuous phase.

As reference materials, polyimide aerogels were also synthesized with surfactant without dispersed phase, and without surfactant and without dispersed phase (neat PI).

2.3. Characterization of oil-in-oil (O/O) emulsions

Interfacial Tension Measurement. The interfacial tension between the dispersed (cyclohexane or n-heptane) and the continuous (DMF) phases was measured using a Du Noy tensiometer (Interfacial Tensiometer 70545, Central Scientific Co., VA). First, the surfactant was dissolved in DMF at concentrations of 0.5, 2.5, and 5.0 vol%. Next, 20 mL of the dispersed phase was gently added to the top of the surfactant solution in DMF by pouring the liquid over a clean glass slide to prevent emulsification and droplet formation during pouring. Interfacial tension was then recorded in triplicate by placing the Du Noy ring at the interface of these two phases.

Emulsion Droplet Size. The droplet size distribution of O/O emulsions (prepared by mixing surfactant, DMF, and cyclohexane/n-heptane) was studied using Olympus BX51 optical microscope (Center Valley, PA). For this purpose, a drop of emulsion was placed on a microscope slide with a depression and its optical images were recorded. The images were analyzed using ImageJ software to yield droplet size distributions from the diameter data of more than 100 droplets.

2.4. Characterization of aerogel foams

Aerogel Foam Morphology and Macrovoid Size Distribution. The morphology of aerogel foams was obtained using a scanning electron microscope (JSM5310, JEOL, MA). An accelerating voltage of 5 kV and emission current of 20 mA was used to capture the SEM images. For this purpose, a representative piece of fractured aerogel foam specimen was mounted on an aluminum stub using carbon tape, followed by sputter coating with silver (ISI-5400 Sputter Coater, Polaron, UK). The macrovoid size distribution was obtained from the analysis of SEM images using ImageJ software. For each specimen, more than 100 macrovoids were considered for determining the macrovoid size distribution. The size of polyimide strands in SEM images was measured using ImageJ software.

IR: Infrared spectra was recorded on a Nicolet iS50 FTIR tri-detector spectrophotometer (Thermo Scientific, MA).

TGA: Thermogravimetric analysis was conducted under N₂ with a Q50 thermogravimetric analyzer (TA Instruments, DE) using a heating rate of 20 °C/min, up to 800 °C.

Porosity and Pore Volume: Porosity was calculated from the values of skeletal (ρ_s) and bulk density (ρ_b) using equation (1). The values of skeletal density were obtained using a helium pycnometer (AccuPyc II 1340, Micromeritics Instrument Corp., GA). Bulk density of the aerogel foams was calculated from the values of mass and volume of the foam specimens.

$$\text{porosity} = (1 - \frac{\rho_b}{\rho_s}) \times 100\% \quad (1)$$

Total pore volume (V_{tot}) was calculated from the bulk and skeletal density according to equation (2):

$$V_{\text{tot}} = \frac{1}{\rho_b} - \frac{1}{\rho_s} \quad (2)$$

Shrinkage: The diameter (d_0) of cylindrical plastic molds for polyimide gels was 13 mm. The diameter shrinkage was calculated from the values of diameter (d) of dried aerogel and d_0 .

BET surface area: Brunauer-Emmett-Teller (BET) surface area of the aerogels and aerogel foams were obtained from N₂ adsorption-desorption isotherms at 77 K using a Micromeritics Tristar II 3020 analyzer

(Micromeritics Instrument Corp. GA).

Gel times and Viscosity: The gel time of the polyimide solution at room temperature was obtained from the crossover point of the storage (G') and loss (G'') moduli measured using an ARES G2 Rheometer (TA Instruments, New Castle, DE). For this purpose, the final reaction mixture was poured into a solvent trap and loaded into the rheometer fitted with a 50 mm cone and plate set up. The rheometer was operated at a constant angular frequency of 1 rad/s at 10% strain.

Compressive Modulus: Compressive modulus of aerogel and aerogel foam specimens were obtained as per ASTM D695-15 method from compressive tests using an Instron 5567 tensiometer (Norwood, MA) fitted with a 1 kN load cell and a compression rate of 1.3 mm/min. Aerogel and aerogel foam specimens were molded into cylindrical shapes with height to diameter ratio of 2:1. The final aerogel specimens were grinded to ensure smooth and parallel surfaces. The compressive modulus value was obtained from the slope of stress vs. strain curves at low strain, typically ~ 0.01 mm/mm.

Contact Angle: The values of contact angle of deionized water were measured using a Rame-hart Model 590 Advanced Automated Goniometer/Tensiometer using the DROPIimage Advanced software (Succasunna, NJ). For this purpose, aerogel specimens were first compressed to remove all the pores before placing water drops on them.

3. Results and discussion

3.1. Emulsion formation

The O/O emulsions prepared from the surfactant and the continuous and dispersed phase liquids were examined to obtain a first approximation of the dispersed phase droplet size distribution in such systems. This was done without any polyimide precursor monomers in the system. Both DMF/cyclohexane and DMF/n-heptane systems exhibited intrinsically low interfacial tension values, respectively at 3.6 and 4.0 mN/m (Table 1). The interfacial tension values reduced to 2.0 and 3.5 mN/m respectively for DMF/cyclohexane and DMF/n-heptane systems with the addition of F127° surfactant. The surfactant concentration above 0.01 vol% had no additional effect on interfacial tension, indicating that surfactant concentrations 0.5, 2.5, and 5.0 vol% were above the critical micelle concentration (CMC). This is in line with other CMC studies of Pluronic® block copolymers in aqueous systems [24].

A continuous phase of the emulsion system was also prepared by mixing DMF, acetic anhydride, pyridine, and F127° in the same proportion as were used later in polyimide gel fabrication. The droplet size distributions for such a system are presented in Fig. 2 as function of surfactant concentration. The values of maximum, minimum, and mean droplet size are listed in Table 2.

Several trends became apparent from the data presented in Fig. 2. The dispersed phase droplets were generally smaller in the case of

Table 1
Interfacial tension of DMF/cyclohexane/F127° and DMF/n-heptane/F127° systems.

Continuous phase	Dispersed phase	Surfactant concentration (vol% of DMF)	Interfacial tension (mN/m)
DMF	cyclohexane	0	3.6 ± 0.1
		0.01	2.0 ± 0.0
		0.5	2.0 ± 0.0
		2.5	2.0 ± 0.1
		5.0	2.0 ± 0.1
	n-heptane	0	4.0 ± 0.0
		0.01	3.5 ± 0.0
		0.5	3.5 ± 0.1
		2.5	3.4 ± 0.1
		5.0	3.4 ± 0.1

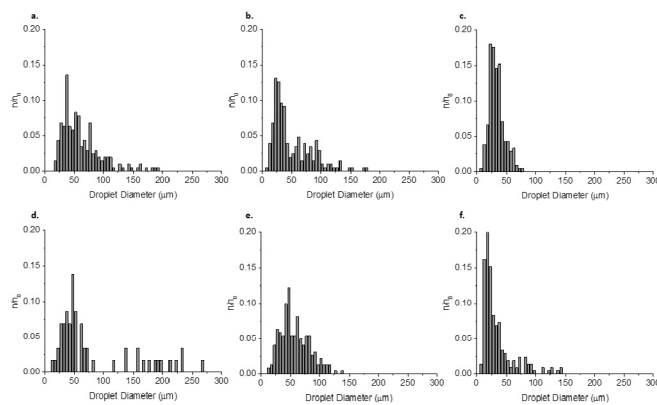


Fig. 2. Droplet size distribution with (a–c) cyclohexane and (d–e) n-heptane as the dispersed phase. Surfactant concentration are (a,d) 0.5 vol%, (b,e) 2.5 vol% and (c,f) 5.0 vol%.

Table 2
Mean, maximum, and minimum droplet size in emulsions.

Surfactant concentration (vol%)	Dispersed phase	Mean droplet diameter (μm)	Maximum droplet diameter (μm)	Minimum droplet diameter (μm)
0.5	cyclohexane	61.7 ± 34.5	191.9	18.6
2.5		50.2 ± 33.5	179.2	8.3
5		33.5 ± 13.0	77.1	9.1
0.5	n-heptane	81.6 ± 67.3	267.6	14.5
2.5		58.0 ± 24.9	135.9	14.7
5		34.7 ± 27.7	141.2	5.8

cyclohexane. It is noted from the data in Table 2 that the maximum droplet diameter for cyclohexane with 0.5 and 2.5 vol% surfactant concentration were 191.9 and 77.1 μm respectively, while the corresponding maximum droplet diameter for the n-heptane system was 267.6 and 141.2 μm respectively. Such a difference in size can be attributed to lower values of interfacial tension in the case of DMF/cyclohexane system, as listed in Table 1. It is intuitive that higher surfactant concentration also led to stabilization of larger interfacial area between the polar and the non-polar phases, resulting in smaller dispersed phase droplets. The mean droplet diameter in the case of DMF/cyclohexane system were 61.7 ± 34.5 μm, 50.2 ± 33.5 μm, and 33.5 ± 13.0 μm respectively for surfactant concentration of 0.5, 2.5, and 5 vol%. A similar trend, i.e., the mean droplet size reduced with an increase of surfactant concentration, is apparent in the case of DMF/n-heptane system.

It is recognized that O/O emulsions have poor stability due to weaker associations of the traditional surfactants at the O/O interface and higher mutual solubility between the dispersed and continuous phases [25]. These inherent characteristics lead to rapid flocculation, coagulation, and ultimately phase separation in O/O emulsion systems, with more significant Ostwald ripening than in aqueous emulsions [26]. This was prevalent in the experimental system considered in this work, as presented in Fig. 3 for the DMF/n-heptane/F127° emulsion with 5 vol% surfactant concentration. The images in Fig. 3 show significant coalescence of the dispersed phase droplets in just 6 s after the emulsion was placed on the optical microscope stage.

The presence of surfactants also increased the viscosity of the continuous phase. Teo and Jana [27] observed an increase of viscosity in solution of F127° surfactant in DMF, e.g., the viscosity increased from 0.87 mPa·s for DMF to 2.3 mPa·s with 5 vol% F127° in solution. Such an increase in viscosity has potential impacts on the diffusion kinetics and the gel time of the polyimide system. The presence of polyimide precursor materials also increases the viscosity of the continuous phase. The higher viscosity of the continuous phase can affect the size of the

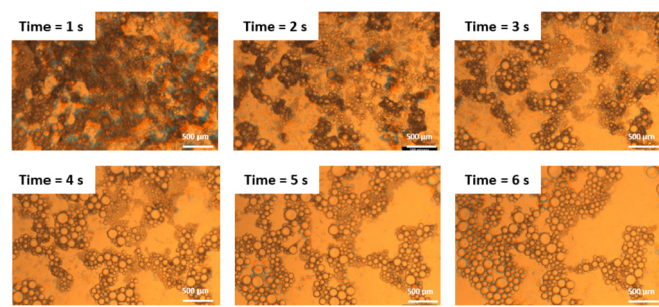


Fig. 3. Optical microscope images of n-heptane/DMF emulsion with 5 vol% F127° surfactant concentration.

dispersed phase droplets in the emulsion and the macrovoids in the gel structures. In view of the above, the morphology of aerogel foam structures is discussed next.

3.2. Morphology of aerogel foam

The aerogel foams primarily consist of macrovoids (as in foams) in a porous polymer domains (as in aerogels). The porous polymer domains in turn are formed by the networks of polymer strands with embedded inherent pore structures. The macrovoids presented in Fig. 4 originated from the dispersed phase liquid droplets in the starting O/O emulsions. Recall that the dispersed phase liquid was replaced by acetone in the solvent exchange step and finally by liquid carbon dioxide in the supercritical drying step. The images presented in Fig. 4 confirm that the macrovoids produced in polyimide aerogel foams had a certain uniqueness. They were not connected by open pores as in polyHIPEs [28] or in emulsion-templated syndiotactic polystyrene (sPS) aerogel foams [20]. However, this type of aerogel foams cannot be strictly classified as closed cell foams as the domains that separate the macrovoids are mesoporous in nature (Fig. 4g). A closer look at Fig. 4g reveals that polyimide strands organized more densely at the macrovoid surface layers than in the bulk. As will be seen later, such dense organization of polymer strands at the macrovoid surface had strong ramifications on specific surface area.

Table 3 lists the data on porosity, pore volume, shrinkage, bulk density, and surface area of aerogel foam materials. Recall that the polymer content in DMF solution was kept constant in all cases at 7.4 wt % and the dispersed phase content was kept constant at 30 vol%, while the concentration of F127° surfactant and type of dispersed phase was varied. It is apparent from the data presented in Table 3 that emulsion-templating with cyclohexane led to an increase of the porosity from 93.7 to 95.5% and corresponding increase in pore volume from 9.3 m³/g to 15.0 m³/g. However, both porosity and total pore volume reduced from 95.5 to 91.4% and from 15.0 to 7.2 m³/g respectively with an increase of surfactant concentration from 0.5 vol% to 5 vol%. We attribute this to diameter shrinkage especially at high surfactant concentrations. The aerogel diameter shrinkage was 11.0% for polyimide with no surfactant compared to 19.2% for an emulsion-templated

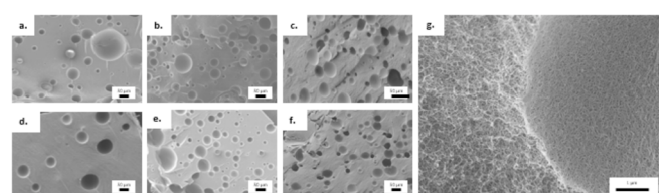


Fig. 4. Emulsion-templated aerogel foams with cyclohexane dispersed phase and surfactant concentration of (a) 0.5 vol%, (b) 2.5 vol% and (c) 5 vol%. The corresponding emulsion-templated aerogel foams with n-heptane are shown in (d–g) at similar surfactant concentrations. (g) Image of the skin layer at the macrovoid surface.

Table 3

Characteristic properties of aerogel foams as function of surfactant concentration.

Surfactant concentration (vol%)	Dispersed phase	Porosity (%)	Total Pore Volume (cm ³ /g)	Shrinkage (%)	Bulk Density (g/cm ³)	Gel Time (mins)	BET Surface Area (m ² /g)	Strand Diameter (nm)
0 (neat PI)	–	93.7 ± 0.0	9.3 ± 0.0	11.0 ± 0.3	0.081 ± 0.000	5.2 ± 0.0	812 ± 13	9.3 ± 1.7
0.5	cyclohexane	95.5 ± 0.2	15.0 ± 0.5	11.1 ± 1.0	0.065 ± 0.002	7.7 ± 0.3	456 ± 6	15.5 ± 3.9
2.5		94.5 ± 0.2	13.1 ± 0.1	15.3 ± 0.5	0.074 ± 0.002	8.6 ± 0.6	363 ± 6	21.1 ± 3.7
5		91.4 ± 0.2	7.2 ± 0.1	19.2 ± 0.0	0.127 ± 0.001	12.4 ± 0.3	285 ± 25	28.1 ± 6.3
0.5	n-heptane	96.0 ± 0.1	17.2 ± 0.0	7.5 ± 0.0	0.056 ± 0.001	10.5 ± 0.5	521 ± 36	15.7 ± 3.0
2.5		95.1 ± 0.1	14.2 ± 0.2	10.9 ± 0.1	0.067 ± 0.001	13.2 ± 0.3	377 ± 21	27.8 ± 4.8
5		92.7 ± 0.2	9.8 ± 0.4	13.3 ± 0.3	0.094 ± 0.002	15.2 ± 0.3	232 ± 3	35.4 ± 6.4

polyimide aerogel foam with 5 vol% surfactant. Another immediate effect of shrinkage is higher bulk density. The bulk density increased from 0.065 to 0.127 g/cm³ as the surfactant concentration was increased from 0.5 vol% to 5 vol%. The n-heptane-templated aerogel foams exhibited similar trends (Table 3).

The DMF and acetone residues in emulsion-templated polyimide gel may be responsible for higher diameter shrinkage observed in the case of aerogel foams. As will be discussed next, the supercritically dried aerogel foams contained residues of surfactants even after several solvent exchange steps. The residual surfactant in turn possibly retained DMF and acetone in the gel, which yielded capillary stress during the supercritical drying step, thus causing collapse of the pore structures and shrinkage of the aerogel foam.

The IR spectra of the neat PI aerogel, aerogel foams and F127[®] surfactants are presented in Fig. 5a. The neat PI aerogel (blue spectra) shows that the imide functional groups were successfully formed as inferred from the presence of absorbance bands at 1716 and 1776 cm⁻¹, corresponding to the symmetrical and asymmetrical stretching of the C=O group, respectively. In addition, the band at 1365 cm⁻¹ is associated with the C-N stretching of the imide rings in the structure. The absence of significant peaks at 2926 and 3273 cm⁻¹, indicative of the COOH and CONH functional groups respectively, confirm that the amic acid functional groups were chemically imidized. The IR spectra for the F127[®] block copolymer surfactant is indicated by the black curve in Fig. 5a. The surfactant is characterized by the peaks at 2880 cm⁻¹ and 1100 cm⁻¹, corresponding to the alkane and ether groups respectively. For aerogel foams, an increase in the absorbance peaks at 2880 and 1100 cm⁻¹ with increasing surfactant concentration indicates retention of surfactant in the aerogel foam structure. Note that the C-O-C peak of the F127 surfactant at 1100 cm⁻¹ overlaps with the imide ring deformation band at the same wavenumber.

The TGA traces presented in Fig. 5b corroborate such a finding. It is noted that degradation of F127[®] surfactant started at around 350 °C (5% weight loss at 393 °C) with no char residue at 800 °C. In contrast, neat PI aerogel monoliths started degradation at 525 °C (5% weight loss at 553 °C) and had a char yield of 58 wt%. The char yield from emulsion-templated aerogel foams at 800 °C varied with surfactant concentration used in the synthesis step. The char yield reduced with an increase of surfactant concentration, e.g., 57, 52, and 44 wt% for surfactant concentrations of 0.5, 2.5, and 5.0 vol% respectively. The above data indicate that emulsion-templated aerogel foams contained residual

surfactant despite repeated washings during the solvent exchange step. The TGA traces in Fig. 5b of the aerogel foams (green, red and yellow curves) do not exhibit distinct weight loss regimes attributed to the residual F127. Instead, they exhibit a distributed departure from the neat PI curve (blue curve) at 450 °C. This is to be expected as polyimide is a good thermal conductor and that some time is required for heat transfer to the surfactant embedded within the structure.

The data in Table 3 also indicate that the presence of surfactants delayed gelation of polyimide in emulsion-templated systems. The gelation time was inferred from the crossover between the storage and loss modulus values (Fig. 6a). The neat PI itself turned into a gel in 5.2 min, while the emulsion-templated systems took 7.7, 8.6, and 12.4 min at surfactant concentrations of 0.5, 2.5, and 5 vol% respectively. As alluded to earlier, the sol-gel transition is a function of the cross-linking reactions. Teo and Jana [27] showed that the gel times in polyimides can be manipulated through two mechanisms. First, a change in the solvent environment can result in a change in the reaction equilibrium and ultimately the conversion in step-growth reactions. It was shown that a more basic solvent environment delays gel times and affects the crosslinking conversion as evident from the mechanical properties. Second, gelation can be prolonged by the addition of a viscosity modifier, such as the F127[®] surfactant used in the current work, that also increases the viscosity, thus inhibiting the diffusion rates of the reactants to the reaction sites. This second approach did not affect the reaction equilibrium and instead helped retain the superior mechanical properties [27]. In the context of the present work, therefore, we assume that the reaction equilibrium was not altered by the use of F127[®] surfactant.

The complex viscosity of all reaction systems increased with time (Fig. 6b) due to crosslinking reactions proceeding in the continuous phase. However, the viscosity increased comparatively slower in emulsion-templated systems.

The BET surface area of aerogel foams reduced with an increase of surfactant concentration in the reaction mixture (Table 3). This can also be seen in the BET isotherms in Fig. 7. The BET surface area reduced from 812 m²/g for neat PI aerogel monolith to 285 m²/g for cyclohexane-templated and 232 m²/g for n-heptane-templated aerogel foam materials at 5 vol% surfactant concentration. The lower surface area in aerogel foams can be attributed to higher density macrovoid skin layers. The macrovoid skin layers were 1–2 strand diameters thick, as

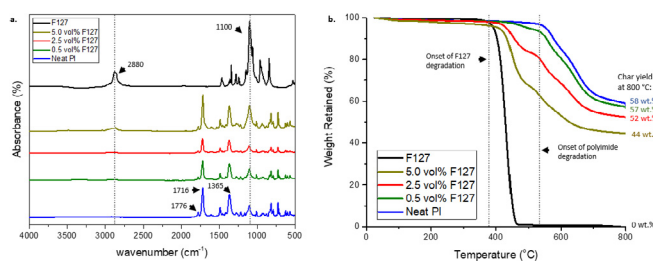


Fig. 5. (a) IR and (b) TGA curves of F127[®], neat PI and emulsion templated aerogel foams.

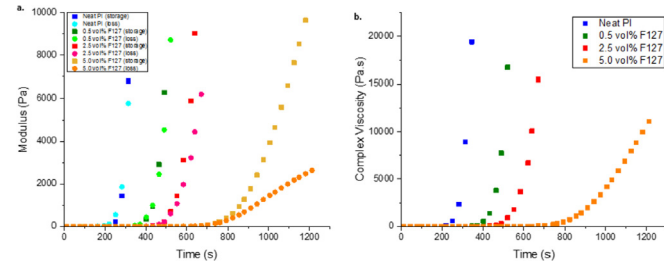


Fig. 6. (a) Storage and loss modulus and (b) complex viscosity of neat PI and emulsion-templated gels.

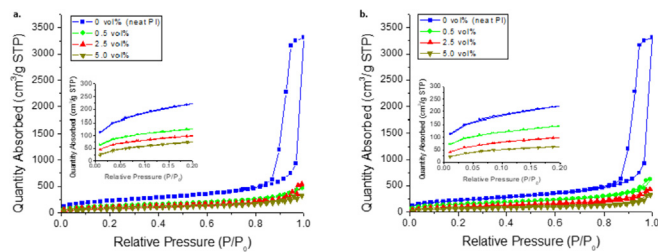


Fig. 7. BET Isotherms of polyimide aerogel foams with varying surfactant concentration with a) cyclohexane and b) n-heptane as dispersed phase.

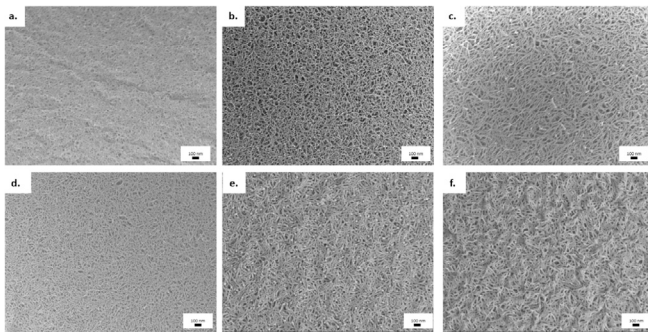


Fig. 8. Representative images of skin layers formed in emulsion-templated aerogel foams with (a-c) cyclohexane and (d-f) n-heptane dispersed phase with surfactant concentration (a,d) 0.5 vol%, (b,e) 2.5 vol% and (c,f) 5 vol%.

evident from Fig. 4g. It was reported earlier for sPS aerogel foams [20] that the skin layers of higher density originate from preferential nucleation of polymer strands at the high energy interfaces, very much akin to expedited heterogeneous separation. The polyimide strands also thickened in the presence of surfactants, resulting in a reduction of specific surface area. This latter factor is supported by the data on polyimide strand diameter (Table 3) gleaned from the SEM images presented in Fig. 8. The mean polyimide strand diameter increased from 9.3 nm for neat PI monoliths to 15.5 nm, 21.1 nm, and 28.1 nm for cyclohexane-templated aerogel foams synthesized with surfactant concentrations of respectively 0.5, 2.5, and 5.0 vol%. The n-heptane-templated aerogel foam systems exhibited even higher diameter polymer strands, e.g., 15.7 nm, 27.8 nm, and 35.4 nm at surfactant concentrations of 0.5, 2.5 and 5.0 vol% respectively. Such a thickening of polymer strands is attributed to a larger gap between the binodal line of liquid-liquid demixing phase separation and the sol-gel transition caused by a reduction in reaction rates due to higher solvent viscosity [29,30].

In this polyimide reaction system, the system first undergoes liquid-liquid demixing, forming both polymer-rich and solvent-rich regions [4]. These regions gradually coarsen to reduce the free energy of the system through reduction of interfacial area between the two phases. As the crosslinking reaction proceeds, the system encounters a sol-gel transition, thus locking the network structure in place. If the reaction rates are reduced through increased viscosity of the system, in this case, via introduction of the surfactant, there is a greater propensity of the two phases to continue coarsening prior to undergoing sol-gel transition, resulting in thicker strands. This was elaborated earlier by Teo and Jana [27] for emulsion-templated sPS aerogel systems.

3.3. Macrovoid size distribution

The final macrovoid size distribution in the aerogel foams resulted from the dispersed phase liquid droplet size distribution in the parent emulsion. Recall that dispersed phase droplets created the macrovoids in the gel and aerogel foams. Therefore, it was expected that the dispersed phase droplet size distributions presented in Fig. 2 would also

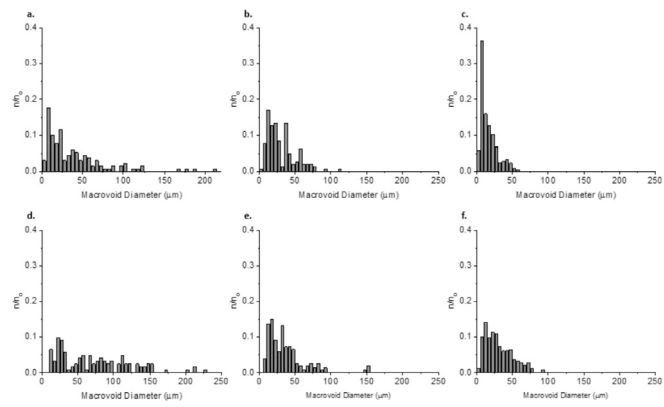


Fig. 9. Macrovoid size distribution with (a-c) cyclohexane and (d-e) n-heptane as the dispersed phase. The surfactant concentration was (a,d) 0.5 vol%, (b,e) 2.5 vol% and (c,f) 5.0 vol%.

map well for macrovoid size distribution in the aerogel foams. From the data in Fig. 9, it is inferred that macrovoid size reduced with an increase of surfactant concentration. The macrovoids found in cyclohexane-templated aerogel foams were consistently smaller than those produced n-heptane-templated system (Table 4). It is worth noting that the macrovoid sizes presented in Fig. 9 and Table 4 are consistently smaller than the emulsion droplets presented in Fig. 2 and Table 2. This can be attributed to the differences in viscosity of the two systems. As explained earlier, the presence of polyimide precursors increased the viscosity of the system as the crosslinking reactions proceeded, as shown in Fig. 6b. This significant increase in viscosity reduced creaming, aggregation, and coalescence rates. In addition, shrinkage up to 19.2% experienced during supercritical drying by aerogel foams is a contributing factor for smaller macrovoid sizes in aerogel foams. It is also noted that the heat from the microscope light used in the characterization of emulsion droplet size in Fig. 2 could also quite possibly facilitate coalescence of droplets in the emulsion systems (without polyimide precursors) at a much faster rate.

3.4. Mechanical properties

The compressive stress vs. strain diagrams of neat polyimide aerogel monolith, polyimide aerogel monolith with surfactant, and emulsion-templated polyimide aerogel monolith are presented Fig. 10a. The compressive modulus values are listed in Table 5. All three compressive stress vs. strain curves exhibit the same shape, with three broad regions. As per Swyngedau [31], the first region (strain 0–0.04 mm/mm) represents the deformation of the original matrix with the applied load borne by the skeletal structure of the crosslinked polymer networks. The second region with strain from 0.04 to 0.7 mm/mm represents the collapse of the skeletal structure and densification of the pores. The third region at strains > 0.7 mm/mm represents almost complete compaction of the pores and the load is now borne by the compressed

Table 4

Average, maximum and minimum macrovoid diameters for emulsion templated aerogel foams.

Surfactant concentration (vol%)	Dispersed phase	Average macrovoid diameter (μm)	Maximum macrovoid diameter (μm)	Minimum macrovoid diameter (μm)
0.5	cyclohexane	39.5 ± 39.0	214	4.6
2.5		30.5 ± 20.1	113	2.9
5		16.5 ± 11.9	59.1	3.3
0.5	n-heptane	72.9 ± 49.6	228	10.8
2.5		36.5 ± 24.7	154	7.1
5		30.8 ± 19.2	95.0	3.7

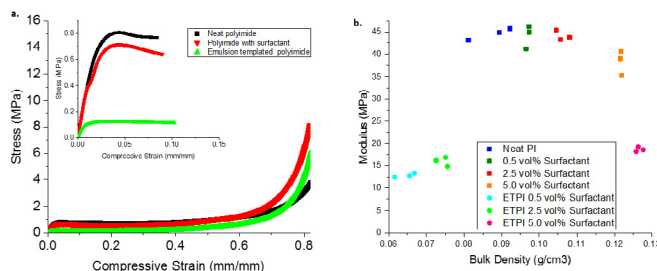


Fig. 10. (a) Compressive stress strain curves and (b) modulus vs bulk density of neat polyimide, polyimide with surfactant and emulsion templated polyimide. Graph in the insert in (a) shows the same samples at low strains of < 0.1.

Table 5

Compressive modulus of neat polyimide, polyimide with surfactant concentration and emulsion templated polyimide.

Surfactant concentration (vol %)	Dispersed Phase	Compressive Modulus (MPa)
0	No	44.5 ± 1.3
0.5		44.1 ± 2.6
2.5		44.1 ± 1.1
5		38.3 ± 2.7
0.5	Yes	12.8 ± 0.5
2.5		16.2 ± 1.4
5		18.9 ± 0.7

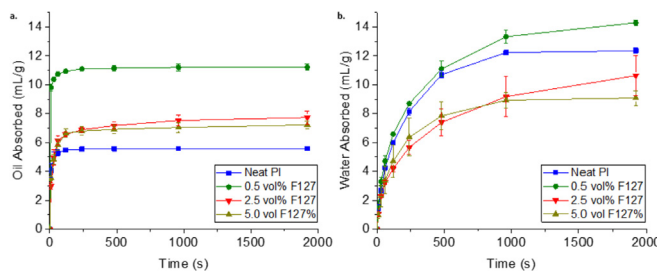


Fig. 11. Oil and water absorption of polyimide and emulsion templated polyimide over time.

bulk polymer. The compressive modulus of the aerogel structure was calculated from the first region of the data; representative stress-strain curves at low strains are provided in the inset in Fig. 10a.

The data presented in Table 5 show that the inclusion of macrovoids through the emulsion-templating process led to a drop of compressive modulus values from 44 MPa to 12.8 MPa owing to reduction of the bulk density of the aerogel foam materials. This trend is also reflected in Fig. 10b. In Fig. 10b, both polyimide with surfactant and emulsion-templated aerogels display similar trends, but at different modulus values. In both cases, the bulk density increases with an increase of surfactant concentration but the compressive modulus is not significantly affected as was earlier reported by Teo and Jana [27]. As discussed earlier, the amount of surfactant retained in the aerogel structures also increased in proportion to the amount of surfactant

taken in the gel precursor materials. We note here that the residual surfactant was dispersed well within the structure and did not provide load bearing capability at low strain regions.

3.5. Oil and water absorption

The macrovoids and the mesoporous structures of aerogel foams contributed to oil absorption capacity. The data presented in Fig. 11 and Table 6 indicate that emulsion templated aerogels were able to absorb up to two times the weight of the oil-phase, i.e., n-heptane compared to the corresponding aerogel monolith. However, aerogel foams produced at higher surfactant concentration absorbed less oil, e.g., 11.2 mL/g at surfactant concentration of 0.5 vol% to 7.7 mL/g at surfactant concentration of 5.0 vol%. We attribute this to greater shrinkage and corresponding reduction in total pore volume from 15.0 to 7.2 m³/g (Table 3). The oil uptake rate first showed an initial jump from 0.16 to 0.35 mL/g-s between polyimide aerogel monolith and emulsion-templated aerogel with 0.5 vol% surfactant concentration. This jump in oil uptake rate can be corroborated with an increase of the water contact angle values from 68.7 to 84.9° (Table 6), attributed to polypropylene hydrophobic groups of the surfactant aggregating on the interfaces and pointing outward, thus increasing the hydrophobic nature of the surface. Note that water contact angle on a melt-pressed film of F127° was 52.4 ± 0.3°. Thus, the use of hydrophobic liquids such as cyclohexane in the dispersed phase during emulsion-templating increased the affinity of PPO segments of F127° molecules to remain at the macrovoid interfaces. This, in turn increased the water contact angle values on compressed aerogel foam specimens. The contact angle values, however, did not change at higher surfactant concentrations.

The presence of macrovoids increased the total water uptake slightly from 12.4 to 14.3 mL/g. In a similar vein, an increase in surfactant concentration in the aerogel foams resulted in a reduction of total water uptake due to increased shrinkage.

Both the oil and water uptake rates reduced with an increase of surfactant concentration. For example, the oil uptake rate for aerogel foams reduced from 0.35 to 0.16 mL/g-s with increasing surfactant concentration. This can be attributed to reduction of micro and mesopores associated with the thickening of the polymer strands as shown in Table 7 [27]. This shift to larger pore sizes would result in a lower capillary pressure, thus reducing the fluid uptake rate. The water uptake rate was also consistently lower than the oil uptake rate due to inherent hydrophobicity of the aerogel foams.

In summary, the macrovoids aid in increasing the total pore volume and act as reservoirs for fluid storage, while the nanometer sized pores of the polyimide aerogel continuous phase provide the capillary pressure for fluid absorption, thus determining the fluid uptake rate.

4. Conclusion

This paper reports successful adaptation of emulsion-templating method for fabrication of aerogel foams from water-sensitive monomers, such as polyimides, using an oil-in-oil emulsion system. The polyimide aerogel foam systems reported in this work exhibited micrometer size voids along with meso and macropores inherent to polyimide aerogels. The block copolymer surfactant stabilized the O/O

Table 6

Oil and water absorption data for neat polyimide and emulsion templated polyimide.

Surfactant Concentration (vol%)	Dispersed Phase	Contact Angle (°)	Oil Absorption		Water Absorption	
			Total Absorbed (mL/g)	Initial rate (mL/g.s)	Total Absorbed (mL/g)	Initial rate (mL/g.s)
0.0	–	68.7 ± 0.8	5.6 ± 0.1	0.16 ± 0.02	12.4 ± 0.2	0.09 ± 0.00
0.5	cyclohexane	84.9 ± 0.9	11.2 ± 0.2	0.35 ± 0.00	14.3 ± 0.2	0.11 ± 0.01
2.5		85.1 ± 2.4	7.7 ± 0.5	0.17 ± 0.02	10.6 ± 1.4	0.08 ± 0.00
5.0		84.2 ± 0.9	7.2 ± 0.3	0.16 ± 0.01	9.1 ± 0.5	0.08 ± 0.03

Table 7

Micro, meso and macropore distribution of emulsion templated polyimide.

Surfactant Concentration (vol%)	Dispersed Phase	Micropore		Mesopore		Macropore	
		Volume (cm ³ /g)	%	Volume (cm ³ /g)	%	Volume (cm ³ /g)	%
0.0	–	0.20	1.48	6.93	51.4	6.42	47.4
0.5	cyclohexane	0.11	0.73	0.52	3.45	14.34	95.82
2.5		0.08	0.62	0.49	3.77	12.51	95.61
5.0		0.05	0.62	0.34	4.67	6.85	94.70

emulsion system, produced smaller size dispersed phase droplets, and thickened the polyimide strands, but did not alter the compressive mechanical properties. The final aerogel foam structures displayed improved oil absorption capabilities due to an increase of pore volume coupled with an increase of hydrophobicity derived from the residual surfactants.

Acknowledgment

This work is partially funded by National Science Foundation under grant number CMMI 1826030.

References

- [1] D. Wilson, H. Stenzenberger, P.M. Hergenrother, *Polyimides*, Chapman and Hall, New York, 1990.
- [2] C.E. Sroog, A.L. Endrey, S.V. Abramo, C.E. Berr, W.M. Edwards, K.L. Olivier, Aromatic polypyromellitimides from aromatic polyamic acids, *J. Polym. Sci.* 3 (4) (1965) 1373–1390, <https://doi.org/10.1002/pola.1996.846>.
- [3] J. Feng, X. Wang, Y. Jiang, D. Du, J. Feng, Study on thermal conductivities of aromatic polyimide aerogels, *ACS Appl. Mater. Interfaces* 8 (20) (2016) 12992–12996, <https://doi.org/10.1021/acsami.6b02183>.
- [4] K. Kawagishi, H. Saito, H. Furukawa, K. Horie, Superior nanoporous polyimides via supercritical CO₂ drying of jungle-gym-type polyimide gels, *Macromol. Rapid Commun.* 28 (1) (2007) 96–100, <https://doi.org/10.1002/marc.200600587>.
- [5] J.N. Guo, B. Nguyen, L.B. Li, M.A.A. Meador, D. Scheiman, M. Cakmak, Clay reinforced polyimide/silica hybrid aerogel, *J. Mater. Chem.* 1 (24) (2013) 7211–7221, <https://doi.org/10.1039/C3TA00439B>.
- [6] M.A.B. Meador, E.J. Malow, R. Silva, S. Wright, D. Quade, S.L. Vivod, H. Guo, J. Guo, M. Cakmak, Mechanically strong, flexible polyimide aerogels cross-linked with aromatic triamine, *ACS Appl. Mater. Interfaces* 4 (2) (2012) 536–544, <https://doi.org/10.1021/am2014635>.
- [7] H. Guo, M.A.B. Meador, L. McCorkle, D.J. Quade, J. Guo, B. Hamilton, M. Cakmak, G. Sprowl, Polyimide aerogels cross-linked through amine functionalized poly-oligomeric silsesquioxane, *ACS Appl. Mater. Interfaces* 3 (2) (2011) 546–552, <https://doi.org/10.1021/am101123h>.
- [8] E.W. M., M.R. Ivan, *Polyimides of Pyromellitic Acid* vol. 14, (1955) US2710853 A, June.
- [9] N. Leventis, C. Sotiriou-Leventis, D.P. Mohite, Z.J. Larimore, J.T. Mang, G. Churu, H. Lu, Polyimide aerogels by ring-opening metathesis polymerization (ROMP), *Chem. Mater.* 23 (8) (2011) 2250–2261, <https://doi.org/10.1021/cm200323e>.
- [10] C. Chidambareswarapattar, Z. Larimore, C. Sotiriou-Leventis, J.T. Mang, N. Leventis, One-step room-temperature synthesis of fibrous polyimide aerogels from anhydrides and isocyanates and conversion to isomorphic carbons, *J. Mater. Chem.* 20 (43) (2010) 9666–9678, <https://doi.org/10.1039/C0JM01844A>.
- [11] J. Kwon, J. Kim, T. Yoo, D. Park, H. Han, Preparation and characterization of spherical polyimide aerogel microparticles, *Macromol. Mater. Eng.* 299 (9) (2014) 1081–1088, <https://doi.org/10.1002/mame.201400010>.
- [12] S. Gu, C. Zhai, S.C. Jana, Aerogel microparticles from oil-in-oil emulsion systems, *Langmuir* 32 (22) (2016) 5637–5645, <https://doi.org/10.1021/acs.langmuir.6b01043>.
- [13] H. Guo, M.A.B. Meador, L. McCorkle, D.J. Quade, J. Guo, B. Hamilton, M. Cakmak, Tailoring properties of cross-linked polyimide aerogels for better moisture resistance, flexibility, and strength, *ACS Appl. Mater. Interfaces* 4 (10) (2012) 5422–5429, <https://doi.org/10.1021/am301347a>.
- [14] M.A.B. Meador, S. Wright, A. Sandberg, B.N. Nguyen, F.W. Van Keuls, C.H. Mueller, R. Rodríguez-Solís, F.A. Miranda, Low dielectric polyimide aerogels as substrates for lightweight patch antennas, *ACS Appl. Mater. Interfaces* 4 (11) (2012) 6346–6353, <https://doi.org/10.1021/am301985s>.
- [15] M.A.B. Meador, E. McMillon, A. Sandberg, E. Barrios, N.G. Wilmoth, C.H. Mueller, F.A. Miranda, Dielectric and other properties of polyimide aerogels containing fluorinated blocks, *ACS Appl. Mater. Interfaces* 6 (9) (2014) 6062–6068, <https://doi.org/10.1021/am405106h>.
- [16] D. Shen, J. Liu, H. Yang, S. Yang, Intrinsically highly hydrophobic semi-alicyclic fluorinated polyimide aerogel with ultralow dielectric constants, *Chem. Lett.* 42 (10) (2013) 1230–1232, <https://doi.org/10.1246/cl.130623>.
- [17] C. Zhai, S.C. Jana, Tuning porous networks in polyimide aerogels for airborne nanoparticle filtration, *ACS Appl. Mater. Interfaces* 9 (35) (2017) 30074–30082, <https://doi.org/10.1021/acsami.7b09345>.
- [18] S. Gu, S.C. Jana, Open cell aerogel foams with hierarchical pore structures, *Polymer* 125 (2017) 1–9, <https://doi.org/10.1016/j.polymer.2017.07.085>.
- [19] X. Wang, S.C. Jana, Tailoring of morphology and surface properties of syndiotactic polystyrene aerogels, *Langmuir* 29 (18) (2013) 5589–5598, <https://doi.org/10.1021/la400492m>.
- [20] N. Teo, S.C. Jana, Open cell aerogel foams via emulsion templating, *Langmuir* 33 (2017) 12729–12738, <https://doi.org/10.1021/acs.langmuir.7b03139>.
- [21] M. S. PolyHIPEs Silverstein, Recent advances in emulsion-templated porous polymers, *Prog. Polym. Sci.* 39 (1) (2014) 199–234, <https://doi.org/10.1016/j.progpolymsci.2013.07.003>.
- [22] M.S. Silverstein, N.R. Cameron, PolyHIPEs—porous polymers from high internal phase emulsions, *Encycl. Polym. Sci. Technol.* (2010), <https://doi.org/10.1002/0471440264.ps571>.
- [23] M. Tebboth, A. Menner, A. Kogelbauer, A. Bismarck, Polymerised high internal phase emulsions for fluid separation applications, *Curr. Opin. Chem. Eng.* 4 (2014) 114–120, <https://doi.org/10.1016/j.coche.2014.03.001>.
- [24] E. Bastrakova, S. Lee, S. Li, A. Venne, V. Alakhov, A. Kabanov, Fundamental relationships between the composition of pluronic block copolymers and their hypersensitization effect in MDR cancer cells, *Pharmaceut. Res.* 16 (1999) 1373–1379, <https://doi.org/10.1023/A:10189428>.
- [25] D. Crespy, K. Landfester, Making dry fertile: a practical tour of non-aqueous emulsions and miniemulsions, their preparation and some applications, *Soft Matter* 7 (23) (2011) 11054–11064, <https://doi.org/10.1039/C1SM06156A>.
- [26] J.A. Marqusee, J. Ross, Kinetics of phase transitions: theory of Ostwald ripening, *J. Chem. Phys.* 79 (1) (1983) 373–378, <https://doi.org/10.1063/1.445532>.
- [27] N. Teo, S.C. Jana, Solvent effects on tuning pore structures in polyimide aerogels, *Langmuir* 34 (2018) 8581–8590, <https://doi.org/10.1021/acs.langmuir.8b01513>.
- [28] N.R. Cameron, D.C. Sherrington, L. Albiston, D.P. Gregory, Study of the formation of the open-cellular morphology of poly(styrene/divinylbenzene) PolyHIPE materials by cryo-SEM, *Colloid Polym. Sci.* 274 (6) (1996) 592–595, <https://doi.org/10.1007/BF00655236>.
- [29] K. Nakanishi, N. Soga, Phase separation in silica sol-gel system containing polyacrylic acid I. Gel formation behavior and effect of solvent composition, *J. Non-Cryst. Solids* 139 (1992) 1–13, [https://doi.org/10.1016/S0022-3093\(05\)80800-2](https://doi.org/10.1016/S0022-3093(05)80800-2).
- [30] H. Li, S. Gu, S. Thomas, T. Liu, S.C. Jana, Investigation of polybenzoxazine gelation using laser light scattering, *J. Appl. Polym. Sci.* 135 (3) (2018) 45709, <https://doi.org/10.1002/app.45709>.
- [31] S. Swyngedau, A. Nussinovitch, M. Peleg, Models for the compressibility of layered polymeric sponges, *Polym. Eng. Sci.* 31 (2) (1991) 140–144, <https://doi.org/10.1002/pen.760310212>.